

## Imaging Offsets in the Moho: Synthetic Tests using Gaussian Beams with Teleseismic Waves

ROBERT L. NOWACK,<sup>1</sup> WANG-PING CHEN,<sup>2</sup> ULRICH KRUSE,<sup>3</sup> and SAPTARSHI DASGUPTA<sup>1</sup>

**Abstract**—We carry out a sequence of numerical tests to understand conditions under which rapid changes in crustal thickness can be reliably imaged by teleseismic body waves. Using the finite-difference method over a 2-D grid, we compute synthetic seismograms resulting from a planar *P*-wavefield incident below the grid. We then image the Moho using a migration scheme based on the Gaussian beam representation of the wavefield. The use of Gaussian beams for the downward propagation of the wavefield is particularly advantageous in certain geologically critical cases such as overthrusting of continental lithosphere, resulting in the juxtaposition of high-velocity mantle material over crustal rocks. In contrast to ray-based methods, Gaussian beam migration requires no special treatment to handle such heterogeneities. Our results suggest that with adequate station spacing and signal-to-noise ratios, offsets of the Moho, on the order of 10 km in height, can be reliably imaged beneath thickened crust at depths of about 50 km. Furthermore, even sharp corners and edges are faithfully imaged when precise values of seismic wave speeds are available. Our tests also demonstrate that flexibility in choices of different types of seismic phases is important, because any single phase has trade-offs in issues such as spatial resolution, array aperture, and amplitude of signals.

**Key words:** Seismic imaging, receiver functions, seismic inversion, migration.

### *Introduction*

Over the past two decades, observations from several different approaches indicate that rapid changes in crustal thickness, of the order of 10 km or more may be common in both modern and relic orogens (HIRN *et al.*, 1984; WHITMARSH *et al.*, 2001; WITTLINGER *et al.*, 2004; ZHU and HELMBERGER, 1998). Offsets in the Moho, if true, have major geodynamic implications, for instance, how are abrupt changes in crustal thickness maintained over geologic time-scales (JIANG *et al.*, 2004; SHAW

---

<sup>1</sup> Department of Earth and Atmospheric Sciences, Purdue University, West Lafayette, IN 47907, U.S.A. E-mail: nowack@purdue.edu

<sup>2</sup> Department of Geology, University of Illinois, Urbana, IL 61801, U.S.A. E-mail: wpchen@uiuc.edu

<sup>3</sup> Department of Physics, University of Illinois, Urbana, IL 61801, U.S.A. E-mail: uek@uiuc.edu

*et al.*, 1992). Longevity of offsets in the Moho certainly implies that mantle portion of the continental lithosphere must be mechanically strong (e.g., BURG *et al.*, 1994; CHEN and YANG, 2004).

Here we report results of a sequence of numerical tests designed to understand conditions under which rapid changes in crustal thickness can be reliably imaged by teleseismic body waves—a necessary step in utilizing dense-spaced, broadband seismic arrays to precisely image key geologic features deep in the lithosphere. Using the finite-difference method, we calculate synthetic seismograms for a suite of models involving different configurations of the Moho. The source of illumination is a planar *P*-wavefield incident from below the lithosphere, a configuration appropriate for earthquake-sources at teleseismic distances. We then image the Moho using a migration scheme based on a Gaussian beam representation of the wavefield.

Such an approach readily handles effects of heterogeneities, arising from certain geologically critical cases such as the thrusting of crustal material under mantle rocks of high seismic wave speeds, which often cause major complications in the seismic wavefield. Our results suggest that Moho disturbances, of the order of 10 km in height, can be detected beneath thickened crust at depths of about 50 km. Such an experimental configuration seems attainable in a number of field experiments that are either ongoing or being planned in the near future, including the mobile component of the USArray under the EarthScope initiative.

### *Migration using Gaussian Beams*

Seismic migration is an imaging procedure that involves the mapping of features on seismic profiles, often displayed as pixels indexed by horizontal distances and arrival times, into subsurface locations of scatterers. Conceptually, a successful trial scatterer position is where the forward-field, propagating from the source of illumination to the scatterers, and the backward-field, propagating from the receivers to the scatterers, coincide (CLAERBOUT, 1976). Under the Born-approximation, this imaging condition is equivalent to applying the adjoint of the linearized, Born scattering operator to the scattered wavefield (TARANTOLA, 2005). The Born approximation linearizes the wave equation with respect to changes in the velocities as  $\delta u = B\delta v$  where  $\delta u$  is the scattered wavefield,  $B$  is the Born operator and  $\delta v$  is the change in the velocities from the background medium. A first-order approximation of the inverse operator can be written as  $\delta v \sim B^*\delta u$  where  $B^*$  is the adjoint of the Born operator. Although this is not an exact inverse, it incorporates the kinematics of the migration operator and is often used in the petroleum industry for structural imaging.

In principle, one can calculate the wavefields used for imaging with a number of techniques. We implement the Gaussian beam (GB) approach for the back-propagating field from the receivers. The use of Gaussian beams distinguishes our

approach from alternative methods such as those by BOSTOCK *et al.* (2001) and BOSTOCK and RONDENAY (1999), who built their algorithms using geometric rays.

A key advantage of using Gaussian beams lies in situations where complications in wavefields result from strong heterogeneities in the medium. Such situations can arise not only in complex geologic settings such as the superposition of the high-velocity mantle material over crustal rocks (Fig. 2) (HIRN *et al.*, 1984; BURG *et al.*, 1994; SHAW, 1992), but also in layered media where strong seismic discontinuities such as the Moho are present.

Under these complications, Gaussian beams (GB) remain single-valued and require no special treatment. For instance, no two-point ray tracing is required, even if triplications develop in the wavefields; and individual Gaussian beams remain finite at caustics, even though our approach is not yet a true amplitude migration. As such, the tests below primarily aim for imaging configuration of complex geological structures, not for recovering material properties. For the sake of brevity, we introduce the salient points of the GB migration below and a brief review of GB in the *Appendix*. A more complete, quantitative overview of GB migration appears in NOWACK *et al.* (2006).

The Gaussian beam imaging approach was initially developed in reflection seismology by HILL (1990, 2001). The seismic wavefields are expanded over a lattice in phase-space, comprised of positions and horizontal wave-numbers. In this formulation, data recorded along the surface (at  $Z = 0$ ) are first decomposed, according to their position ( $X$ ), by applying a sequence of local Gaussian windows (Fig. 1A). In the next step, windowed data are slant-stacked along slant-angles,  $\theta$ , which is related to the horizontal wavenumber ( $k$ ). The windowed slant-stacks constitute an overdetermined collection (“frame”) of elements representing the original data.

These stacks of the data are then back-propagated in the aperture ( $X-Z$ ) plane as paraxial Gaussian beams according to their positions ( $X$ ) and angles ( $\theta$ ) (NOWACK, 2003). Finally, the wavefield at the scatterer is formed by superposing all propagated beam-components of the data. In the *Appendix*, the imaging formulation, Equations (A3) and (A4), are analogous to that given by HILL (2001) for pre-stack migration of seismic reflection profiles under the configuration of a common-source gather and surface source. In our case, Equations (A3) and (A4) are appropriate for illumination from below by a teleseismic  $P$ -wave source.

To visualize the application of GB migration, Figure 1B shows an example of an image formed by using just a single Gaussian beam. The data are full synthetic seismograms calculated for the overhang model in Figure 2, with the target being illuminated by a planar  $P$ -wave, whose initial angle of incidence is  $15^\circ$  counter-clockwise from the vertical. Between depths of about 40 and 60 km, an incomplete image, mostly for the dipping portion of the Moho, already begins forming by using the  $P_s$  phase with only a single GB beam. The feature above the depth of 20 km is a false image that is successfully eliminated when a full set of beams are utilized (cf. Fig. 5A).

### Frame Based Gaussian Beam Decomposition

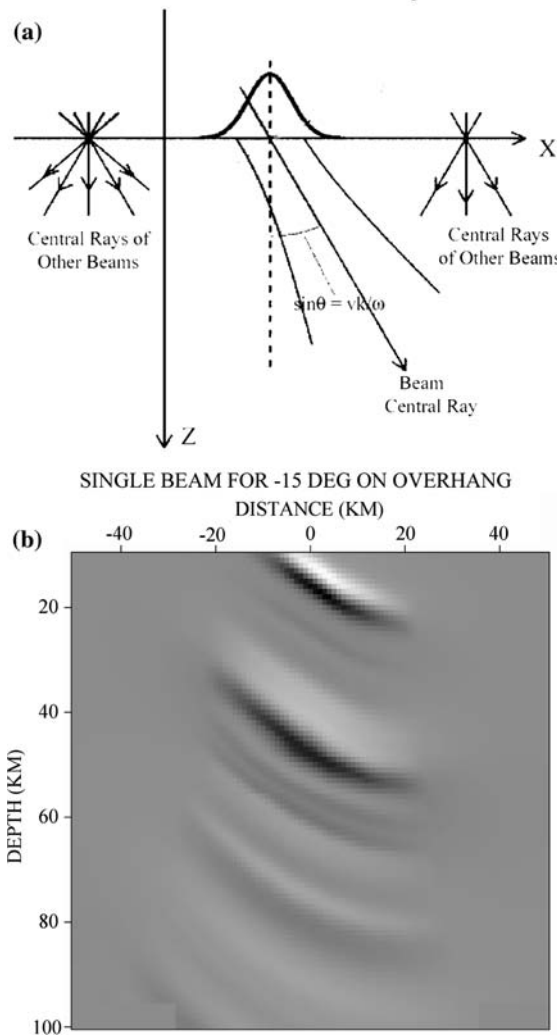


Figure 1

Diagrams illustrating basic concepts of Gaussian beam (GB) migration. (A) The wavefield observed at the surface (at  $Z = 0$ ) is decomposed by applying a sequence of local Gaussian windows along positions on the surface ( $X$ ). The windowed data are then slant-stacked according to the slant-angle  $\theta$ . The windowed slant-stacks constitute an overdetermined collection ("frame") of elements representing the original data. These stacks of the data are then back-propagated in the aperture ( $X-Z$ ) plane as paraxial Gaussian beams according to their positions ( $X$ ) and angles ( $\theta$ ). The plot shows the trajectory of a single GB initiating at a specific position and angle, where the angle  $\theta$  is specified in terms of the horizontal wavenumber  $k$ , the wavespeed  $v$ , and the angular frequency  $\omega$ . In the notation used in the text,  $k = \omega p_l^q$ , where  $p_l^q$  is the horizontal slowness or ray-parameter. (B) An example of imaging using just a single GB-component of the observed wavefield. The target structure is an overhang in the Moho (Fig. 2), already emerging from this incomplete image. The illumination is a planar  $P$ -wave from below, whose initial angle of incidence is  $15^\circ$  counterclockwise from the vertical.

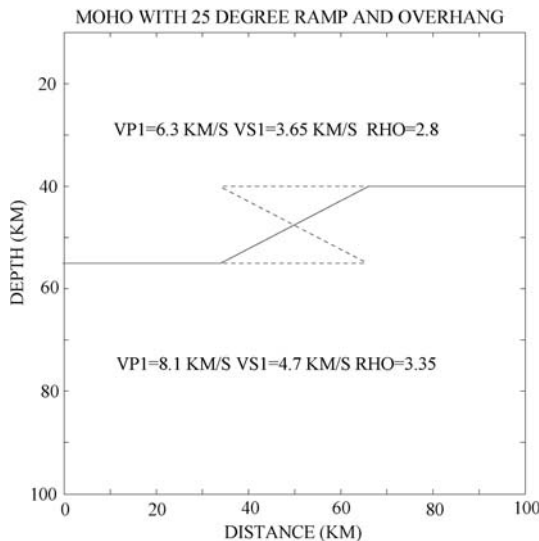


Figure 2

Examples of crustal models tested. The two cases show a ramp (solid curve) and an overhang (dashed curve) in the Moho discontinuity. In both cases, the inclined portion of the Moho dips at 25° but at opposite directions. Parameters for the crust are:  $P$ -wave speed ( $V_P$ ), 6.10 km/s;  $S$ -wave speed ( $V_S$ ), 3.65 km/s; and density, 2800 kg/m<sup>3</sup>. Corresponding values for the mantle are:  $V_P$ , 8.10 km/s;  $V_S$ , 4.70 km/s; and density, 3350 kg/m<sup>3</sup>. In both cases, the flat-lying portions of the Moho are at depths of 55 km and 40 km.

### Numerical Tests

To simulate a range of Moho configurations in response to lithospheric-scale faulting, we tested several two-dimensional models where the offset of the Moho is approximated by a ramp and an overhang. Geological examples of a ramp-like Moho include the junction of the Gulf of Genoa and southernmost Corsica (from seismic refraction profiles, GALSON and MUELLER, 1987) and the northern edge of the Tibetan plateau (based on a small number of transmitted  $P$  arrivals from teleseismic distances, ZHU and HELMBERGER, 1998). Similarly, examples of an overhang exist beneath the Central and Eastern Alps (from seismic refraction/wide-angle reflection profiles, SCARASCIA and CASSINIS, 1997) and in central Australia (based on seismic reflection and gravity profiles, SHAW *et al.*, 1992).

Figure 2 shows two models where the inclined portion of the Moho dips at 25° for either a ramp or an overhang. The array is illuminated from below by planar  $P$ -wavefields with different angles of incidence. For each model, we calculate synthetic seismograms for a receiver array of 200 km in aperture and a station-spacing ( $\Delta x$ ) of 1 km. This value is appropriate to avoid spatial aliasing, governed approximately by the inequality:  $\Delta x \leq V_{\min}/(2f_{\max})$ , where  $V_{\min}$  is the minimum wave

speed in the medium and  $f_{\max}$  is the maximum frequency of interest (IKELLE and AMUNDSEN, 2005). For models shown in Figure 2,  $V_{\min} = 3.65$  km/s and the initial pulse-width is about 1 s, so a station spacing of 1 km is more than sufficient.

We use a finite-difference method based on the velocity-stress formulation of Virieux and Madariaga (see, VIRIEUX, 1988). In addition, we apply absorbing boundary conditions along the bottom of the grid and use a large padding zone on both sides of the grid to minimize artifacts caused by grid edges. For the overhang model illustrated in Figures 2, 3A and 3B show examples of synthetic seismograms on the vertical and the horizontal component, respectively. In this particular case, the incident wave comes up from the bottom of the grid at  $15^\circ$  clockwise from the vertical-up direction and has an initial waveform of a Gaussian pulse  $G(l) = e^{-l^2/2\sigma^2}$ , where  $l$  is distance from the center of the pulse and  $\sigma = 2.15$  km.

To accentuate arrivals in the coda, Figures 3A and B are plotted using a grey-scale with automatic gain control (AGC), a standard practice in exploration seismology, even though actual imaging was performed using true amplitudes. Several features are apparent in Figure 3. For the direct  $P$  arrival, there are two line segments of smooth move-out, with a subtle shift near the middle of the array. These features correspond to two limbs of flat-lying Moho straddling a zone of abrupt change in crustal thickness (Fig. 2).

Multiple conversions and reflections off the Moho and the free-surface are apparent, manifesting themselves as subparallel traces across Figures 3A and 3B. Some key arrivals include the direct  $P$  phase, the  $Ps$  phase (primary conversion of  $P$  to  $SV$  across the Moho), the  $PpPp$  phase ( $P$  phase reflected off the free-surface then scattered off the Moho as a  $P$  phase), and the  $PpPs$  phase (similar to the  $PpPp$  phase except scattered off the Moho as an  $SV$  phase). In addition, sharp corners and edges in the model produce complex patterns of diffraction, roughly in the form of hyperbolas, akin to those on unmigrated reflection seismic profiles. We have carefully examined all synthetic seismograms, making sure that numerical noise such as numerical dispersion, grid anisotropy, and effects arising from grid boundaries are minimal.

We then apply the Gaussian beams migration to synthetic seismic profiles, using a grid spacing of  $1 \text{ km} \times 1 \text{ km}$  for the scatterers. In principle, one can choose any number of different seismic phases to perform the migration. In practice, we focus on the first three prominent coda phases following the direct  $P$ -arrival, the same choices as in conventional receiver-function analysis (e.g., AMMON *et al.*, 1990).

As a first example, we apply GB migration to synthetic seismograms corresponding to the ramp structure shown in Figure 2, with the incident plane wave coming up at  $15^\circ$  clockwise from the vertical. The image in Figure 4A is formed from the horizontal component of the seismic profile, assuming that all scattering is associated with  $P-SV$  conversion or the  $Ps$  phase. For comparison, the image in Figure 4B is formed from the vertical component of the seismic profile, assuming that all scattering is equivalent to the  $PpPp$  phase. In both cases, the geometry of the

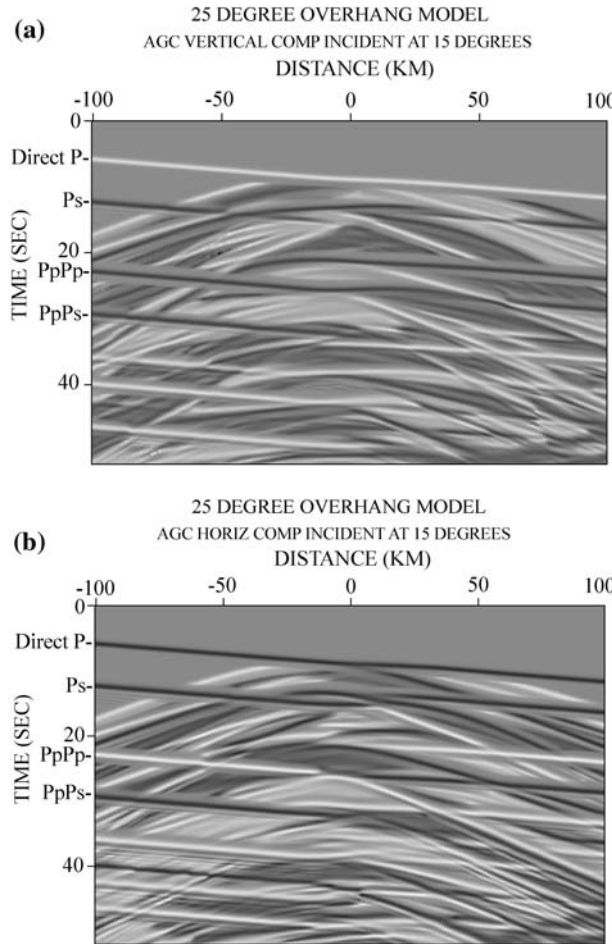


Figure 3

Examples of synthetic seismograms generated by the finite-difference method. Panels (A) and (B) show seismic profiles, each sampled at a station spacing of 1 km and extending over an array aperture of 200 km, of the vertical and horizontal component of ground motion, respectively. For plotting purposes, we apply automatic gain-control to each seismic profile. The model has an overhang in the Moho (Fig. 2) and the illumination is a planar  $P$ -wave from below, with an initial angle of incidence at  $15^\circ$  clockwise from the vertical. The direct  $P$ -arrival is approximately a Gaussian pulse with dominate frequencies up to about 1 Hz. Some key phases are labeled. Notice complex patterns of diffraction (convex-up curves) due to sharp edges and corners in the model.

Moho is successfully recovered by the migration which correctly collapses complex patterns of diffraction into a ramp for the Moho.

Recall that although the mathematical formulation and computation are involved, one can view the migration as a way to map various arrivals in time into correct spatial positions of scatterers. In doing so, the late-arriving  $PpPp$

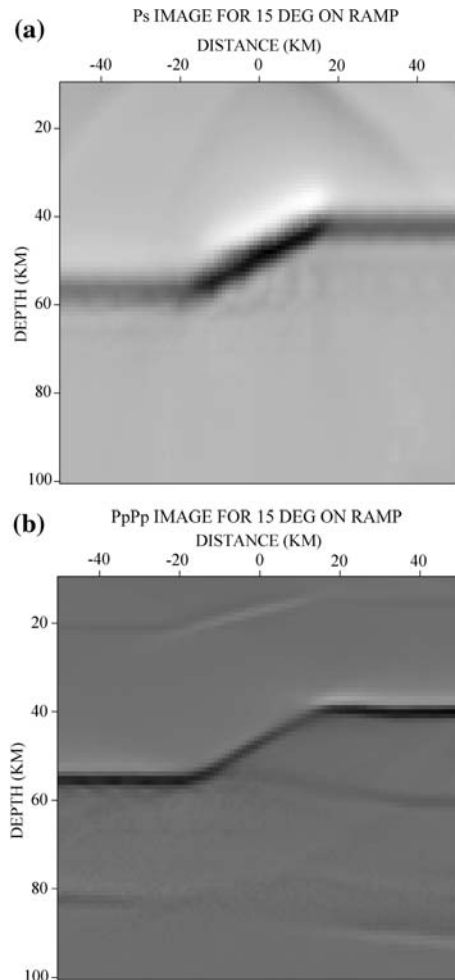


Figure 4

Results of Gaussian beam migration, imaging the ramp-like structure of the Moho shown in Figure 2. The illumination is a planar  $P$ -wave from below, with an initial angle of incidence at  $15^\circ$  clockwise from the vertical. Panels (A) and (B) show images assuming that all scattering is due to the  $Ps$  and the  $PpPp$  phase, respectively. Both images are faithful, with high resolution in depth in the latter case.

phase requires less stretching than the  $Ps$  phase which immediately follows the direct  $P$  phase, resulting in better vertical resolution in the former case (Figs. 4A and 4B).

This conclusion is a noteworthy point of departure from conventional practices which rely heavily on the  $Ps$  phase because of its high amplitude on the radial component of data (AMMON *et al.*, 1990). While high signal-to-noise ratio of the  $Ps$  phase is an advantage, there are counteracting limitations. For instance, the isolation

of the  $P_s$  phase generally requires all three components of data, and the interpretation of results depends on knowledge of both  $P$ - and  $S$ -wave speeds ( $V_p$  and  $V_s$ ). In contrast, utility of the  $PpPp$  phase requires only the vertical component of data and knowledge of  $V_p$  (TSENG and CHEN, 2006).

In practice, LI and NÁBELEK (1999) showed discernable  $PpPp$  phases across a broadband profile in Cascadia, however their results were limited to low-frequency signals (below about 0.2 Hz). Lately, TSENG and CHEN (2006) used  $PpPp$  phases from a short-period array to image the Moho in southern India, extending the range of useable frequencies to as high as 1.2 Hz. As such, improved vertical resolution offered by the  $PpPp$  phase further bolsters the value of this phase to complement conventional approaches (Fig. 4). We also perform migrations assuming all signals are from the  $PpPs$  phase. The results correctly reproduce the ramp in Moho but show interference from other late arrivals for this particular Moho depth in our crustal model.

Results of the migration are equally successful for the more complex model of an overhang in the Moho, with repeated juxtaposition of crustal and mantle materials (Fig. 2). In Figures 5A and 5B we show resulting images of such an overhang that can be directly compared with corresponding images of the ramp (Figs. 4A and 4B). To facilitate such comparisons, the incident wave used to produce Figures 5A and 5B comes up at  $15^\circ$  counter-clockwise from the vertical. This illumination is comparable to that of the case shown in Figure 4 because in both cases, the incident wave vector has a horizontal component parallel to the up-dip direction of structures being imaged. Notice that even acute angles associated with the overhang are faithfully imaged by our technique (Figs. 5A and 5B). As in the case of a ramp (Fig. 4), the late-arriving  $PpPp$  phase offers better vertical resolution than the  $P_s$  phase.

As a further comparison, Figure 5C shows the migrated image of the overhang with an illumination angle at  $15^\circ$  clockwise from the vertical. The overall geometry of the Moho is correct but the dipping portion of the structure is now barely imaged. This issue is a direct consequence of the fact that the last leg of the  $PpPp$  phase now reflects off the dipping Moho toward the down-dip direction of this strong interface, pointing scattered wavefronts away from the center of the array.

For the  $PpPp$  phase, straightforward geometry leads to the following approximate relationships among angles of incidence at the free surface ( $i$ ), dip angle of the interface ( $d$ ), average depth of the interface ( $h$ ), and required half-aperture of the array ( $L_{1/2}$ ):

$$L_{1/2} \sim h \tan(2d - i), \quad (1a)$$

and

$$L_{1/2} \sim h \tan(2d + i), \quad (1b)$$

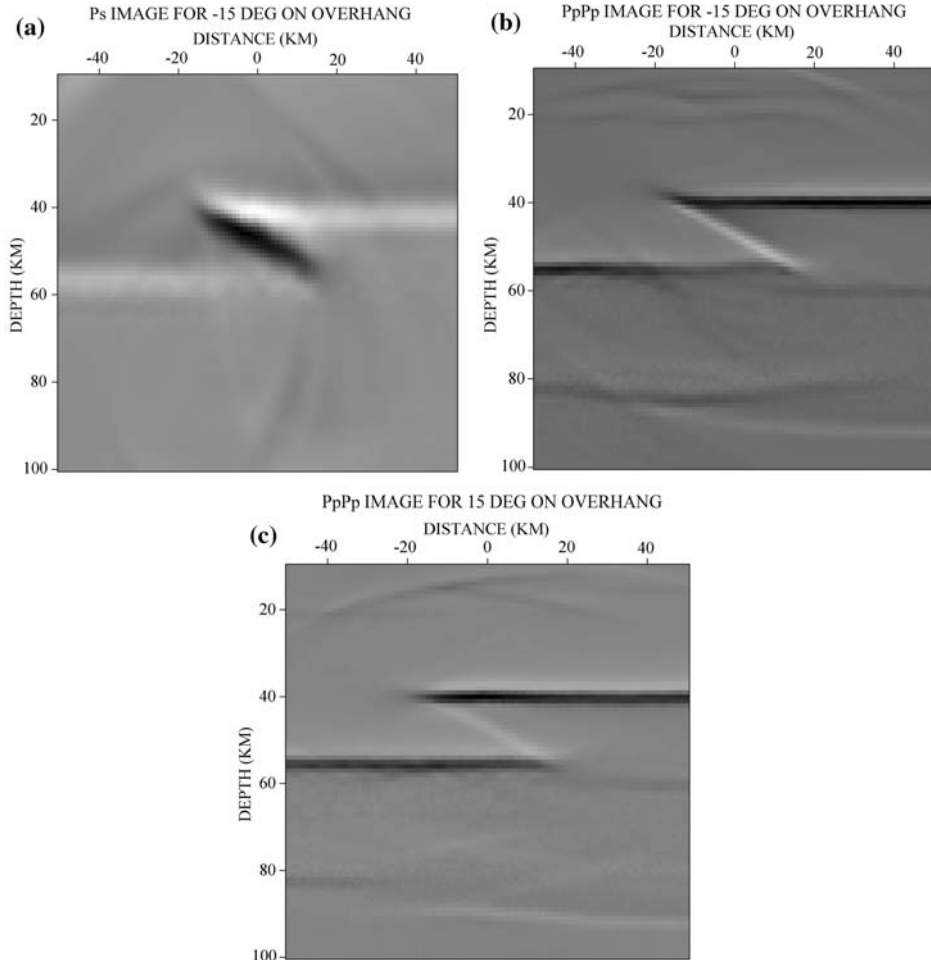


Figure 5

Results of Gaussian beam migration, imaging the overhang of the Moho shown in Figure 2. Panels (A) and (B) show images assuming that all scattering is due to the  $Ps$  and the  $PpPp$  phase, respectively. In both cases, the illumination is a planar  $P$ -wave from below, with an initial angle of incidence at  $15^\circ$  counter-clockwise from the vertical. Both images successfully recovered salient features in this complex model where juxtaposition of crustal and mantle material appears more than once at acute angles. Like the cases shown in Figure 4, panel (B) has high resolution in depth. Panel (C) shows an image assuming that all scattering is due to the  $PpPp$  phase but the illumination has an initial angle of incidence of  $15^\circ$  clockwise from the vertical. In this case, signals reflected off the dipping interface are lost beyond the finite aperture of the recording array, resulting in a deteriorated image of the dipping Moho.

if the incident wave vector has a horizontal component parallel to the up-dip and down-dip direction of the structure, respectively. Corresponding conditions for the  $PpPs$  phase are slightly less restrictive than Equations (1a) and (1b), but only the  $Ps$

phase, whose path is simple and steep in the crust, is largely unaffected by the finite length of the receiver array. However, the vertical resolution of the  $P_s$  phase is lower than phases reflected off the free-surface (Figs. 4A and 5A). These considerations call for the combined use of all available seismic phases for imaging based on passive earthquake sources.

In practical terms, with an array aperture of 200 km, deep-seated structures that exist at depths of approximately 50 km below the center of the array will be successfully imaged only if the dip of the target structure is less than about  $25^\circ$ . As such, steep dipping structures such as an abrupt step in the Moho can only be inferred by comparing shallow-dipping segments nearby (cf. ZHU and HELMBERGER, 1998, who modeled a small number of the direct  $P$  phase.)

### *Discussion*

Since the Moho is a strong seismic discontinuity, any disturbance of this interface results in large deviations from layered structures of seismic wave speeds

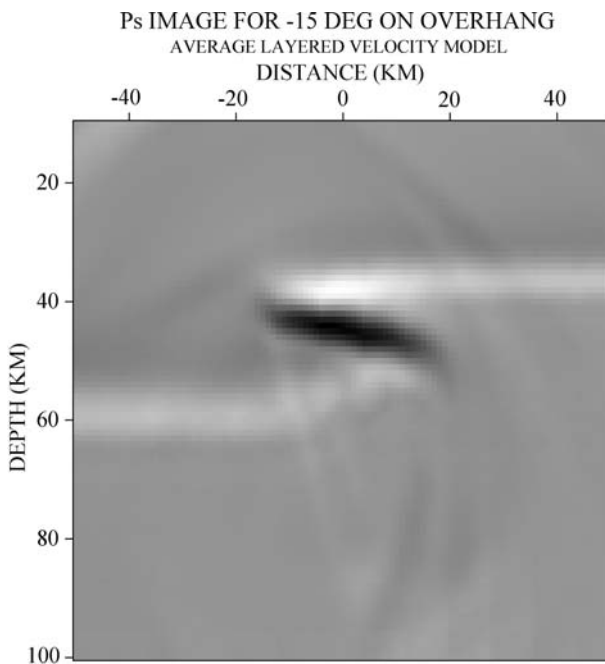


Figure 6

An example of distortions in imaging by using an incorrect model for seismic wave speeds. This image is comparable to that in Figure 5A, except here we assume a layered structure of seismic wave speeds, with a flat-lying Moho at a depth of 47.5 km. There are pull-up and pull-down in the Moho, resulting in distortions of the overhang.

(Fig. 2). For cases discussed to date, we assume that the velocity model is known. To illustrate the effect of large lateral variations in seismic wave speeds, Figure 6 shows the migrated image of the Moho overhang by assuming an incorrect, layered velocity model with a uniform crustal thickness of 47.5 km. On one hand, the result is promising in that the overall configuration of an overhang is recovered. On the other hand, not all details are exact. For instance, long wavelength pull-ups and pull-downs are apparent for the flat-lying portions of the Moho. There are also short-range distortions in the image, particularly below the overhang where the wave velocities undergo large, complex changes.

To improve the fidelity of migration, one could first perform travel-time tomography by using local and regional seismic phases (e.g., IYER and HIRAHARA, 1993). An alternative approach being developed in the petroleum industry is a joint analysis of migration and velocity (MVA) in which the velocity model is iteratively updated by examining the consistency among results from different image gathers (e.g., AL-YAHYA, 1989; LIU and BLEISTEIN, 1995). The velocity model is then iteratively updated as part of the imaging process. To adapt MVA using teleseismic earthquakes as sources of illumination, one would require multiple teleseismic events over a wide range of distances (equivalent to variations in angles of incidence), and this is a direction of further research.

### Conclusions

To test procedures that can reliably imaging rapid changes in crustal thickness using teleseismic body waves, we apply migration based on Gaussian beams to synthetic seismograms that are generated from the finite-difference method. The use of Gaussian beams in migration has advantages in allowing for heterogeneous geologic structures and triplications in scattered wavefields. The migration formulism is also flexible in choices regarding types of scattered waves for imaging, including direct conversion such as the  $P_s$  phase and reflected phases such as  $PpPp$  and  $PpPs$ .

We test crustal models that range from gentle ramps to sharp overhangs in the Moho. At depths of about 50 km beneath thickened crust, migration can resolve offsets in Moho of about 10 km in height. More important, we successfully image intricate structures such as overhangs in Moho that are expected to accompany lithospheric-scale thrust faulting. In general, it is advantageous to use a combination of phases for seismic imaging based on passive (earthquake) sources. For instance, the  $P_s$  phase is not particularly sensitive to aperture of the recording array while phases such as  $PpPp$  and  $PpPs$  provide superior vertical resolution.

## Appendix

### Overview of Gaussian Beam Migration Using Teleseismic Body Waves

For completeness, a brief overview of Gaussian beam migration using teleseismic body waves is provided in this Appendix. A more detailed discussion can be found in Nowack *et al.* (2006).

In a heterogeneous elastic medium, the Green's function, representing a propagating wave from an initial position  $\underline{x}^g$  to a final position  $\underline{x}'$ , can be expanded as a sum of Gaussian beams (ČERVENÝ *et al.*, 1982; ČERVENÝ, 1985a,b; 2000; Nowack, 2003):

$$g_{ij}(\underline{x}', \underline{x}^g; \omega) = \int d\underline{\gamma} \Psi(\underline{\gamma}, \omega) u_{ij}^{gb}(\underline{x}', \underline{x}^g, \underline{\gamma}, \omega) \quad (\text{A1})$$

where  $u_{ij}^{gb}$  are the individual Gaussian beams,  $\Psi(\underline{\gamma}, \omega)$  are weighting functions, and  $\underline{\gamma}$  specifies the ray coordinates (for example, a ray with take-off angle  $\theta$ ) for the beams. Eqn. (A1) can be used to describe either the *P*- or *S*-wave components of the Green's function in the far-field.

Each individual Gaussian beam solution can be written as

$$u_{ij}^{gb}(\underline{x}', \underline{x}^g, \underline{\delta}, \omega) = U_{ij}^{gb}(\underline{x}', \underline{x}^g, \underline{\gamma}) e^{i\omega(T(\underline{x}', \underline{x}^g, \underline{\gamma}) - t)}, \quad (\text{A2})$$

where  $U_{ij}^{gb}(\underline{x}', \underline{x}^g, \underline{\gamma})$  is the beam's amplitude, including geometric spreading, any reflection/transmission coefficients, ray-dependent radiation patterns of the source, and polarization vector at positions along the beam's central ray.

For a beam solution, the phase term  $T(\underline{x}', \underline{x}^g, \underline{\gamma})$ , expanded to second-order away from the central ray, is real along the central ray and complex at positions off the central ray. The curvature matrix (used to describe the phase away from the central ray) is complex and positive-definite; and its real-part represents the curvature of the wavefront while the imaginary-part tapers the amplitude away from the central ray, thus forming a beam. By applying a paraxial or second-order approximation of the phase function away from the central ray, no two-point ray tracing is required for positions off the central ray. For the amplitude term, the geometric spreading is also complex, but it remains nonsingular along the entire beam even at caustics.

The Gaussian beam imaging formulation for the scattering of *SV*-waves from heterogeneities illuminated by incident *P*-waves can be obtained by applying the adjoint of the Born-approximation operator and expanding the scattered *SV*-waves into Gaussian beams (for more details, see Nowack *et al.*, 2006):

$$I(\underline{x}') \sim \sum_L \int d\omega/(2\pi) C_1(\omega) \bar{S}(\omega) \bar{u}_i^0(\underline{x}', p_1^E, \omega) \int \frac{dp_1^g}{dp_3^g} \bar{\Psi}(p_1^g, \omega) \bar{u}_{il}^{gbSV}(\underline{x}', x^L, p_1^g, \omega) D(x^L, p_1^g, p_1^s, \omega), \quad (\text{A3})$$

where  $I(\underline{x}')$  is the image (obtained from the adjoint of the Born-approximation operator) of the perturbed shear modulus from a background medium (taken to be a Poisson solid here). The summation is over the discretely sampled beam centers with a spacing of  $\Delta L$ , where  $x^L = L\Delta L$ . In addition,  $C_1(\omega) = -3(\omega/V_p)^2 \frac{\Delta L}{\sqrt{2\pi}\sigma}$  is a coefficient, where  $\sigma$  is the initial beam width at the receivers, being specified at a reference frequency.

The integration over frequency ( $\omega$ ) results from the specific imaging condition adopted here. In the integrand,  $\bar{u}_i^0(\underline{x}', p_1^E, \omega)$  is the complex conjugate of the incident  $P$ -wavefield at the scatterer locations  $\underline{x}'$ , where  $p_1^E$  is the horizontal component of the slowness vector for the incident  $P$ -wave and  $\bar{S}(\omega)$  is the source-time function where the overbars signify complex conjugates.  $p_1^g$  represents the horizontal component of the slowness vector along the seismograph array (specified at the beam centers), and  $\bar{u}_{il}^{gbSV}$  are the complex conjugate of the individual Gaussian beam components for the scattered  $SV$ -wave.

Finally,  $\bar{\Psi}(p_1^g, \omega)$  is the complex conjugate of the weighting function in Eqn. (A1), indexed in 2-D by the horizontal component of the slowness. In the end, a summation is performed on the subscripts  $i$ , where a near-vertically incident  $P$ -wave has  $i = 3$ . Also, in equation (A3)

$$D(x^L, p_1^g, p_1^E, \omega) = \int dx^g \delta u_1(x^g, p_1^E, \omega) e^{-(x^g-x^L)^2/2\sigma^2} e^{j\omega p_1^g(x^g-x^L)} \quad (\text{A4})$$

representing local slant-stacks of the horizontal-component of the data,  $\delta u_1(x^g, p_1^E, \omega)$ , in the  $x^g$ -coordinate along the surface where data have been Gaussian windowed at distances  $x^L = L\Delta L$ . The horizontal component of the slowness vector is related to the take-off angle  $\theta$  at the seismograph array by  $p_1^g = \sin \theta / V_S$ . The terms that propagate the windowed and slant-stacked data downward into the subsurface are simply the paraxial Gaussian beams  $\bar{u}_{il}^{gbSV}(\underline{x}', x^L, p_1^g, \omega)$  for the case of scattered  $SV$ -wave observed at the receivers. Equations (A3) and (A4) are similar to those given by HILL (2001) for pre-stack migration of seismic reflection data under the configuration of a common-offset gather using surface sources.

## REFERENCES

- AKI, K. and RICHARDS, P., *Quantitative Seismology* (Freeman, San Francisco, 1980).  
 AL-YAHYA, K. A. (1989), *Velocity analysis by iterative profile migration*, Geophysics 54, 718–729.

- AMMON, C. J., RANDALL, G. E., and ZANDT G. (1990), *On the nonuniqueness of receiver function inversions*, J. Geophys. Res. 95, 15303–15318.
- BOSTOCK, M.G. and RONDENAY, S. (1999), *Migration of scattered teleseismic body waves*, Geophys. J. Int. 137, 732–746.
- BOSTOCK, M. G., RONDENAY, S., and SHRAGGE, J. (2001), *Multiparameter two-dimensional inversion of scattered teleseismic body waves I. Theory for oblique incidence*, J. Geophys. Res. 106, 30,771–30,782.
- BURG, J. P., DAVY, P., and MARTINOD, J. (1994), *Shortening of analog models of the continental lithosphere – new hypothesis for the formation of the Tibetan Plateau*, Tectonics 13, 475–483.
- ČERVENÝ, V. (1985a), *Gaussian beam synthetic seismograms*, J. Geophys. 58, 44–72.
- ČERVENÝ, V., *The applications of ray tracing to the numerical modeling of seismic wavefields in complex structures*, In *Seismic Shear Waves* (ed. G. Dohr) (Geophysical Press, London, 1985b) pp. 1–124.
- ČERVENÝ, V., *Seismic Ray Theory* (Cambridge University Press, 2000).
- ČERVENÝ, V., POPOV, M. M., and PŠENČÍK, I. (1982), *Computation of wavefields in inhomogeneous media – Gaussian beam approach*, Geophys. J.R. Astr. Soc. 70, 109–128.
- CHEN, W. P. and YANG, Z. H. (2004), *Earthquakes beneath the Himalayas and Tibet: Evidence for strong lithospheric mantle*, Sci. 304, 1949–1952.
- CLAERBOUT, J.F., *Fundamentals of Geophysical Data Processing*, (McGraw-Hill, New York, 1976).
- GALSON, D.A. and MUELLER, S., *The European Geotraverse (EGT) Project*, A progress report. In *Composition, Structure and Dynamics of the Lithosphere-Asthenosphere system* (eds. Fuchs K., and Frodevaux C.) (Am. Geophys. Union, Washington, D.C., 1987) pp. 253–272.
- HILL, N.R. (1990), *Gaussian beam migration*, Geophysics 55, 1416–1428.
- HILL, N.R. (2001), *Prestack Gaussian beam depth migration*, Geophysics 66, 1240–1250.
- HIRN, A., LEPINE, J. C., JORBERT, G., SAPIN, M., WITTLINGER, G., XU, Z., GAO, E., WANG, X., Teng, J., XIONG, S., PANDEY, M., and TATER, J. (1984), *Crustal structure and variability of the Himalayan border of Tibet*, Nature 307, 23–25.
- IKELLE, L.T. and AMUNDSEN, L., *Introduction to Petroleum Seismology*, (Society of Exploration Geophysicists, Tulsa, OK, 2005).
- IYER, H. M. and HIRAHARA, K. (eds.), *Seismic Tomography Theory and Practice* (Chapman and Hall, New York, 1993).
- JIANG, X.D., JIN, Y., and McNUTT, M. K. (2004), *Lithospheric deformation beneath the Altyn Tagh and West Kunlun faults from recent gravity surveys*, J. Geophys. Res. 109, B05406, doi:10.1029/2003JB002444.
- LI, X.-Q. and NÁBELEK, J.L. (1999), *Deconvolution of teleseismic body waves for enhancing structure beneath a seismic array*, Bull. Seismol. Soc. Am. 89, 190–201.
- LIU, Z. Y. and BLEISTEIN, N. (1995), *Migration velocity analysis – Theory and iterative algorithm*, Geophy. 60, 1034–1037.
- NOWACK, R. L. (2003), *Calculation of synthetic seismograms with Gaussian beams*, Pure Appl. Geophys. 160, 487–507.
- NOWACK, R. L., DASGUPTA, S., SCHUSTER, G. T., and SHENG, J. M. (2006), *Correlation migration using Gaussian beams of scattered teleseismic body waves*, Bull. Seism. Soc. Am. 96, 1–10.
- SCARASCIA, S. and CASSINIS, R. (1997), *Crustal structures in the central-eastern Alpine sector: a revision of the available DSS data*, Tectonophysics 271, 157–188.
- SHAW, R.D., GOLEBY, B. R., KORSCH, R.J., and WRIGHT, C., *Basement and cover thrust tectonics in central Australia based on the Arunta-Amadeus seismic-reflection profile*. In *Basement Tectonics 9* (eds. M.J. Rickard, H.J. Harrington, and P.R. Williams) (Kluwer Academic Pub., Dordrecht, 1992) pp. 55–84.
- TARANTOLA, A., *Inverse Problem Theory* (SIAM, Philadelphia, 2005).
- TSENG, T.-L. and CHEN, W.-P. (2006), *Probing the southern Indian shield with P-wave receiver-function profiles*, Bull. Seismol. Soc. Am. 96, 328–333.
- VIRIEUX, J. (1988), *P-SV wave propagation in heterogeneous media: Velocity-stress finite-difference method*, Geophy. 51, 889–901.
- WHITMARSH, R. B., MANATSCHAL, G., and MINSHUL, T. A. (2001), *Evolution of magma-poor continental margins from rifting to seafloor spreading*, Nature 413, 150–154.

- WITTLINGER, G., VERGNE, J., TAPPONIER, P., FARRA, V., POUPINET, G., JIANG, M., SU, H., HERQUEL, G., and PAUL, A. (2004), *Teleseismic imaging of subducting lithosphere and Moho offsets beneath western Tibet*, Earth and Planetary Sci. Lett. 221, 114–130.
- ZHU, L. and HELMBERGER, D. V. (1998), *Moho offset across the northern margin of the Tibetan Plateau*, Sci. 281, 1170–1172.

(Received August 1, 2006, accepted February 9, 2007)

Published Online First: July 4, 2007

---

To access this journal online:

[www.birkhauser.ch/pageoph](http://www.birkhauser.ch/pageoph)

---